energies

MDPI

Article

Design of a Bearingless Outer Rotor Induction Motor

Yuxin Sun, Jingwei Tang * and Kai Shi

School of Electrical and Information Engineering, Jiangsu University, Zhenjiang 212013, China; syx4461@ujs.edu.cn (Y.S.); shikai80614@163.com (K.S.)

* Correspondence: 2221507019@stmail.ujs.edu.cn; Tel.: +86-157-0610-7126

Academic Editor: Frede Blaabjerg

Received: 16 December 2016; Accepted: 11 May 2017; Published: 17 May 2017

Abstract: A bearingless induction (BI) motor with an outer rotor for flywheel energy storage systems is proposed due to the perceived advantages of simple rotor structure, non-contact support and high speed operation. Firstly, the configuration and operation principle of the proposed motor are described. Then several leading dimensional parameters are optimally calculated for achieving the maximum average values and the minimum ripples of torque output and suspension force. Finally, by using the finite element method, the characteristics and performance of the proposed machine are analyzed and verified.

Keywords: bearingless motor; finite element analysis; induction motor; motor optimization design; outer rotor

1. Introduction

Due to their merit of high power density, high and super-high speed motors have attracted more and more attention for a lot of industry applications [1]. However, the conventional high speed motor usually suffers from some inevitable disadvantages which limit its development and application, such as friction, acoustic noise and the need for regular lubrication because of the adoption of mechanical bearings. Fortunately, magnetic bearings have been proposed in recent years, so that motors with non-contact support, namely magnetic bearing motors, can be produced to avoid the problems caused by mechanical bearings. However, conventional magnetic bearing motors are usually bulky, and require a number of wiring connections as well as many single phase inverters [2].

Based on the similarities between the configurations of magnetic bearing and conventional electric machines, a variety of bearingless machines have been presented and widely investigated, such as bearingless induction (BI) motors [3], bearingless permanent magnet motors [4], superconducting bearingless machines [5] and bearingless switched reluctance generators [6], in which a set of suspension winding (SW) is embedded in the stator slots along with the conventional armature winding. Bearingless motors therefore possess a series of advantages compared to magnetic bearing motors, such as shorter shafts, higher critical speed, and more applicability for demanding super-high speed operation. Compared to the other types of bearingless motors, BI motors have the merits of simpler rotor structures, lower cost and higher reliability. In [7], the axial oscillation production mechanism of a BI motor with a skewed internal rotor was analyzed, based on which an improved configuration with two tandem rotors skewed in opposing directions was presented to cancel the axial forces. In [8], a three-phase BI motor with divided windings was proposed and an independent control method for each phase was employed to enhance its fault tolerance capability.

In this paper, a BI motor with an outer rotor for flywheel energy storage systems is proposed. The motor configuration is shown and its operation principle explained in Section 2. In Section 3, the optimization design of the proposed machine is discussed and its characteristics are analyzed by using the finite element analysis (FEA) method. Then the key dimensional parameters and

electromagnetic performance features are presented in Section 4. Finally, some conclusions are drawn in Section 5.

2. Motor Configuration and Operation Principle

Figure 1 shows the proposed BI motor with outer rotor, in which a squirrel-cage rotor is adopted. It can be seen that the configuration is very similar to that of a conventional outer rotor induction motor. The key difference is that there are two sets of 3-phase windings, namely the SW and the traditional armature winding, named torque winding (TW) in this paper, placed in the stator slots. Furthermore, in order to reduce the iron losses in the rotor core and pulsating losses in the tooth portion, half-closed pear-shaped slots with small slot openings are adopted in the stator.

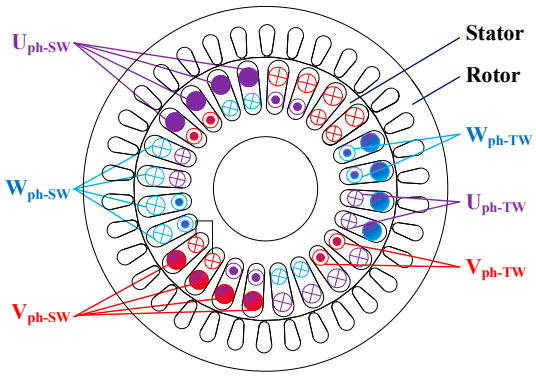

Figure 1. Configuration of proposed bearingless outer rotor induction motor.

The rotor suspension of the bearingless motor is achieved based on the Maxwell electromagnetic force due to the resultant field produced by two sets of windings with a different number of poles. To realize stable suspension of the rotating rotor, it is necessary to produce an additional and controllable radial force, so that a unilateral magnetic pull force can be achieved to overcome the external load in the radial direction. By feeding a suitable current into the SW, the balance and symmetry of the rotating magnetic field produced by the TW in the motor airgap can be disturbed. In other words, the magnetic fields in some partial areas of the airgap are enhanced and those in the corresponding symmetrical areas can be weakened due to the contribution of the suspension current. Thus, a radial resultant force, namely a suspension force, is produced in the direction of the enhanced magnetic field. According to the bearingless motor principle, the pole pair numbers of two sets of windings and their electrical frequencies must satisfy Equation (1):

$$P_t = P_s \pm 1,\ \omega_s = \omega_t \tag{1}$$

where P_s, P_t, ω_s and ω_t are the pole-pair numbers and electrical frequencies of SW and TW, respectively.

In this paper, P_t = 2 and P_s = 1. When the corresponding currents are fed into the two sets of windings, the theoretical magnetic field distributions of proposed BI outer rotor motor can be depicted as in Figure 2, in which ψ_t and ψ_s represent the flux linkage produced by the TW and the SW, respectively.

As shown in Figure 2a, the torque and suspension magnetic fields can be produced by the equivalent torque and suspension currents, respectively, which are drawn using dashed lines and full lines, respectively. It can be seen that the directions of the two magnetic fields in area A are the same, so the resultant magnetic field in area A equals the sum of ψ_t and ψ_s. On the other hand, the two magnetic field directions are opposed in area B, thus the total magnetic field in area B is reduced due to ψ_s. Thus a suspension force in the X-axis positive direction F_x can be obtained. By feeding a reverse current into the SW, the direction of ψ_s is reversed, so that a suspension force in the opposite

direction $-F_x$ can be realized. Similarly, the suspension force F_y and $-F_y$ can be performed by adjusting the current phases of two sets of windings, as shown in Figure 2b. So, it can be concluded that by feeding currents with different phases into the SW and the TW, a suspension force in any direction can be obtained.

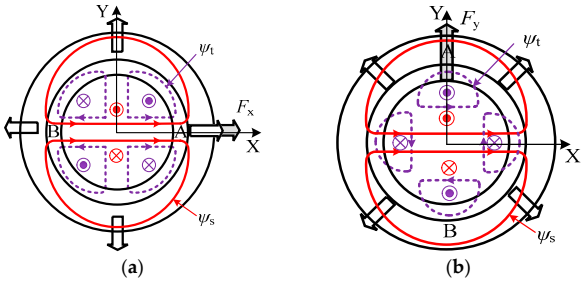

Figure 2. Principle of suspension force generation. (**a**) *x*-direction; (**b**) *y*-direction.

When the rotor is concentric with the stator, the Maxwell magnetic suspension forces per area acting on the rotor can be expressed as:

$$\begin{cases} F_x = F_M \cos(\lambda - \mu) \\ F_y = -F_M \sin(\lambda - \mu) \end{cases} \tag{2}$$

$$F_M = \frac{\pi P_t P_s \psi_t \psi_s}{18 \mu_0 l_a r N_t N_s} \tag{3}$$

where μ_0 is the airgap permeability, l_a is the motor stack length, r is the inner radius of the rotor, N_s and N_t are the winding turn numbers of SW and TW, respectively, λ and μ are the initial phase angles of magnetic field produced by the SW and the TW, respectively, and F_M, F_x and F_y are the suspension force magnitude and the suspension force components in the *X*- and *Y*-axis directions.

Then, a stable suspension force can be obtained from (2) and (3), in which the suspension force direction is determined by the angle difference between λ and μ. And the suspension force magnitude can be controlled by Equation (3).

Ignoring the coupling between two windings, the electromagnetic torque can be expressed by Equation (4):

$$\begin{aligned} T &= T_t + T_s \\ &= \frac{6 l_a r \mu_0}{\pi g_0} \left[P_t N_t^2 \left(i_{tsq} i_{trd} - i_{tsd} i_{trq} \right) + P_s N_s^2 \left(i_{ssq} i_{srd} - i_{ssd} i_{srq} \right) \right] \end{aligned} \tag{4}$$

where the 1st term T_t and the 2nd term T_s are the torques produced by the TW and the SW, respectively, i_{trd}, i_{trq} and i_{srd}, i_{srq} are the rotor induction currents in the *d*-*q* coordinate due to the torque current and suspension current, respectively, i_{tsd}, i_{tsq} and i_{ssd}, i_{ssq} are the torque current and suspension current, respectively, in the *d*-*q* coordinate, g_0 is the airgap length.

Figure 3 shows the torque waveforms, in which T is the torque produced by both SW and TW. It can be seen that T is almost equal to the sum of T_t and T_s, which is consistent with the result of (4). T_s is very small compared to T_t in this paper.

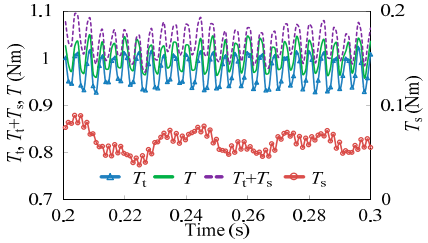

Figure 3. Torque waveforms.

When the rotor is eccentric, the flux is not balanced anymore. Then a unilateral magnetic pull force due to the rotor eccentricity will act on the rotor [9]. In the case of rotor eccentricity, the radial suspension force of bearingless motors can be expressed as:

$$\begin{cases} F_{\mathrm{x}} = k_{\mathrm{i}} i_{\mathrm{td}} \psi_{\mathrm{td}} + k_{\mathrm{m}} x \\ F_{\mathrm{y}} = k_{\mathrm{i}} i_{\mathrm{tq}} \psi_{\mathrm{tq}} + k_{\mathrm{m}} y \\ k_{\mathrm{i}} = \frac{\pi P_{\mathrm{t}} P_{\mathrm{s}} L_2}{8 l r \mu_0 N_{\mathrm{t}} N_{\mathrm{s}} k_{\mathrm{t}} k_{\mathrm{s}}} - \frac{3 P_{\mathrm{t}} N_{\mathrm{s}} k_{\mathrm{s}}}{4 r N_{\mathrm{t}} k_{\mathrm{t}}} \end{cases} \tag{5}$$

where k_{i} is the radial force stiffness, k_{t} and k_{s} are the winding coefficient of TW and SW, respectively, ψ_{td} and ψ_{tq} are the d- and q-axis components of airgap flux linkage produced by TW, respectively, k_{m} is related to the motor structural parameters, L_2 is the SW mutual inductance, $i_{s\mathrm{d}}$ and $i_{s\mathrm{q}}$ are the d- and q-axis components of suspension current, respectively, x and y are the rotor radial eccentric displacement in the X- and Y-axis directions, respectively.

3. Optimized Design

Table 1 shows the design specification of proposed BI outer rotor motor. In order to design and analyze the proposed motor, a two-dimensional FEA model is built in the finite element software of MagNet®. It should be mentioned that the rotor mass is less than 5.0 kg considering the adjustment of rotor parameters, so the motor is required to produce at least a 50 N suspension force when the rotor is concentric with the stator. Considering the ripple range of suspension force, the minimum suspension force is selected to be higher than 55 N.

Table 1. Design specification of proposed BI outer rotor motor.

Definition	Requirement
Out power, P_N (kW)	≥1.5
Rated speed, n (r/min)	15,000
Output torque, T_{ave} (Nm)	≥1
Torque ripple, T_{rip}	≤20%
Suspension force, F_{ave} (N)	≥55
Suspension force ripple, F_{rip}	≤10%
Rotor weight, m (kg)	5.0

As shown in Table 2, according to the design methods mentioned in [10,11], the initial parameters of the motor are determined. Then the optimization using the FEA is carried out to realize the maximum average values and the minimum ripples of torque output and suspension force. In the process of optimization, the stator outer radius, the stator stack length, the rotor outer radius and the stator slot number are 38 mm, 70 mm, 57 mm and 24, respectively, and unchanged.

Table 2. Initial dimension parameters.

Items	Values
Airgap, g_0 (mm)	0.3
Stator pole arc coefficient, c	0.9
Stator outer diameter, D_s (mm)	76
Stator stack length, l_{a} (mm)	70
Stator slot number, Z	24
Number of rotor bar	30
Rotor outer diameter, D_{r} (mm)	117
Stator tooth shoe thickness, t_{s} (mm)	0.4
Bar dimension, R_{a} (mm)	1.5
Bar dimension, L (mm)	5.5

In order to optimize the structure parameters, which have a great influence on the motor, the single parameter optimization method [12] is used in this paper. Based on the FEA model, several key dimension parameters are defined, as shown in Figure 4. The design and optimization flow chart is shown in Figure 5. The initial values and optimal ranges, such as stator pole arc coefficient, radius and length of rotor slot, stator tooth shoe thickness, and so on are shown in Table 3. It should be mentioned that the suspension force is assumed to be in the *X*-axis positive direction and the rotor is concentric with its stator in the optimization design.

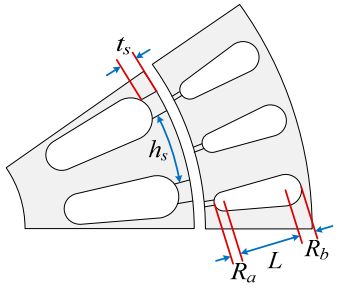

Figure 4. Parameter definition of proposed BI outer rotor motor.

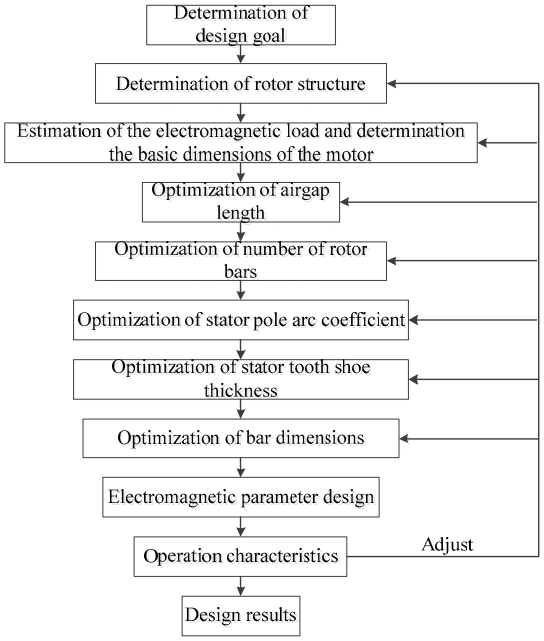

Figure 5. Design and optimization flow chart.

Table 3. Initial values and optimal range.

Items	Initial Values	Range
Number of rotor bar	30	28–34
Stator pole arc coefficient, c	0.9	0.8–1.0
Stator tooth shoe thickness, t_s (mm)	0.4	0.1–0.7
Bar dimension, R_a (mm)	1.5	1.3–2
Bar dimension, L (mm)	5.5	5–7

Firstly, the average suspension force F_{ave}, is calculated with different airgap lengths and different suspension currents. As shown in Figure 6, when the suspension current is less than 3 A, the suspension force reduces significantly with the increase of the airgap length. On the other hand, firstly, when the

current is between 0 A to 3 A, the suspension force increases linearly with the different airgap lengths and the increase of suspension current. Then, the suspension force decreases due to the saturation of iron core. When the airgap length is 0.2 mm and the current equals 3 A, the maximum suspension force occurs. Taking the manufacture difficulty into account, the airgap length is selected to be 0.3 mm in this paper.

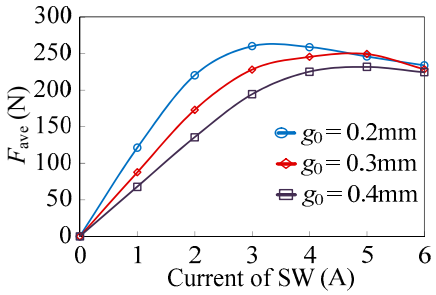

Figure 6. F_{ave} with different airgap lengths versus suspension current.

Figure 7 depicts the relationship between the suspension force and the rotor bar number, in which the subscripts of ave and rip represent the average and ripple values, respectively. It is shown that F_{ave} and F_{rip} increases and reduces, respectively, with the increase of number of rotor bars. Then the torque output is also analyzed with different rotor bar numbers. As shown in Figure 8, the average torque T_{ave} is almost the same with different bar numbers. It is worth to be mentioned that the torque ripple T_{rip} with 2n bars is obviously higher than that with 2n + 1 bars, where n is a positive integer.

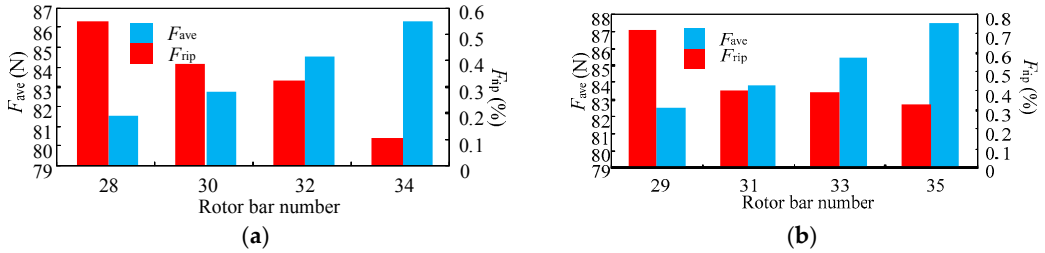

Figure 7. F_{ave} and F_{rip} versus rotor bar number. (**a**) Even number of rotor bar; (**b**) Odd number of rotor number.

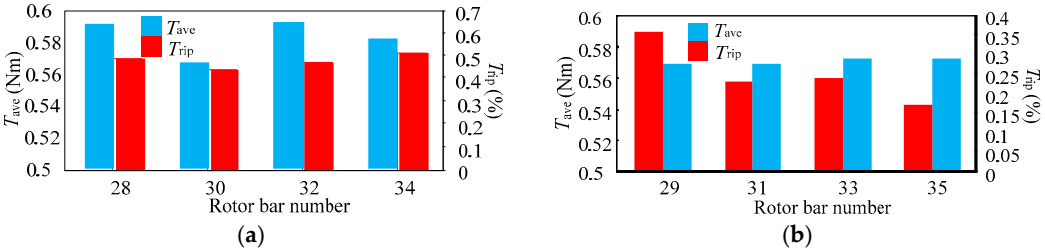

Figure 8. T_{ave} and T_{rip} versus rotor bar number. (**a**) Even number of rotor bar; (**b**) Odd number of rotor number.

Then, the stator pole arc coefficient, which is defined as the ratio between the stator tooth shoe arc length h_s and the stator tooth pitch, is optimized. As shown in Figure 9, T_{rip} and T_{ave} decrease and increase monotonously, respectively, with the increase of stator pole arc coefficient. Figure 10 shows the relationship between suspension force and stator pole arc coefficient. It can be found that the stator pole arc coefficient has little influence on F_{ave}, while the suspension force ripple reaches the minimum

value of 10.8% when the stator arc coefficient equals 0.99. When the stator pole arc coefficient equals 0.93, the suspension force reaches the maximum value of 106 N.

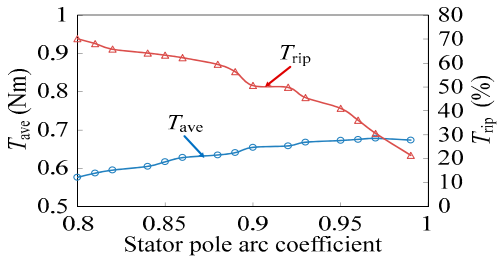

Figure 9. T_{ave} and T_{rip} versus stator pole arc coefficient.

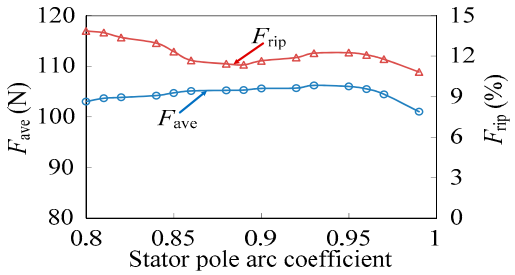

Figure 10. F_{ave} and F_{rip} versus stator pole arc coefficient.

Figure 11 compares the torques at different stator tooth shoe thickness t_s. It can be seen that T_{rip} reaches a minimum value of 9.13% when t_s is 0.35 mm. However, T_{ave} increases linearly with the increase of stator tooth shoe thickness below 0.35 mm and then tends to be constant. Figure 12 shows the suspension force variation waveforms with t_s. It illustrates that F_{ave} increases continuously along with the increase of t_s. Meanwhile, the suspension force ripple fluctuates around 13%.

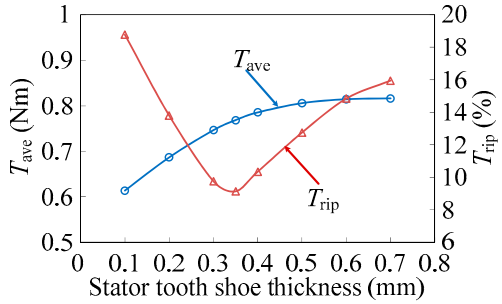

Figure 11. T_{ave} and T_{rip} versus stator tooth shoe thickness.

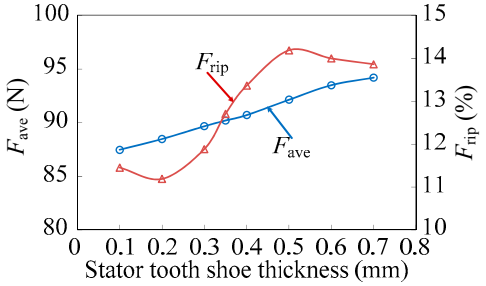

Figure 12. F_{ave} and F_{rip} versus stator tooth shoe thickness.

According to the operation principle of induction motors, when a symmetrical three-phase current is fed into the armature winding, a rotating magnetic field will be generated. As the rotor speed is less than the speed of rotating magnetic field, induction current and back EMF are generated in rotor bars. Due to the interaction between stator magnetic field and rotor current, torque output can be generated. It should be noted that the shape of rotor bars, as well as that of the rotor slots, is one of the main factors affecting the induced current, thus influencing the performances of induction motors, such as starting current, slip, efficiency, temperature, power factor, etc. So, it is very important to optimize the dimension parameters of rotor slots, namely R_a, R_b and L, to obtain the optimal performances of torque and suspension force.

As shown in Figure 13, T_{ave} of the presented motor enhances when R_a and L increase. However, T_{rip} reduces with the increase of R_a as shown in Figure 14. It should be mentioned that R_b is selected to be (R_a + 0.4) mm in this paper to reduce the optimization difficulty.

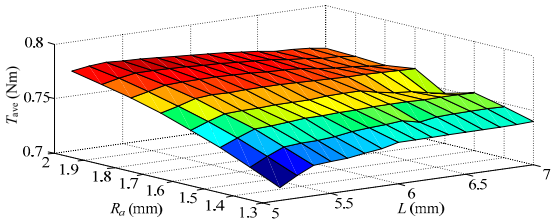

Figure 13. T_{ave} variation waveforms versus bar dimensions.

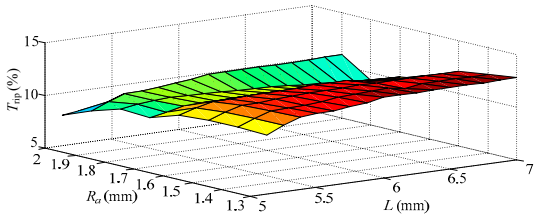

Figure 14. T_{rip} variation waveforms versus bar dimensions.

As shown in Figures 15 and 16, F_{ave} reduces with the increase of R_a and L. Meanwhile, the suspension force ripple fluctuates around 15%.

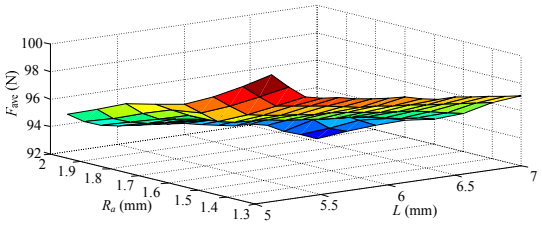

Figure 15. F_{ave} variation waveforms versus bar dimensions.

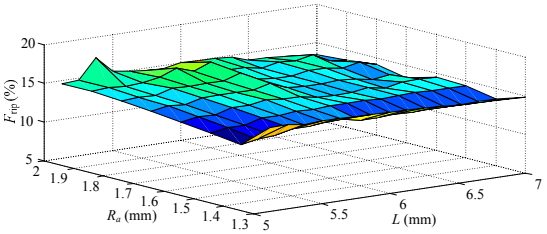

Figure 16. F_{rip} variation waveforms versus bar dimensions.

In the design of this motor, not only the torque and torque ripple need to be considered, but also the suspension force and suspension force ripple need to be taken into account. When the rotor rotates at high speed, the suspension force generated by the motor will be able to overcome the gravity of the rotor. The ripple of suspension force decides the complexity of suspension force control algorithm. If the suspension force ripple were reduced sufficiently in motor design stage, the motor control algorithm will be greatly simplified and the stability of motor operation will be improved. Therefore, torque, torque ripple, suspension force, suspension force ripple are the four goals of our first choice optimization.

Once the four optimization objectives are determined, the corresponding optimization model $f(x_i)_{min}$ can be proposed. As presented in (6), $f(x_i)_{min}$ is considered as a weighted sum of each optimization objective [13]. Generally, the optimization design needs to obey some constraints. In this paper, the motor is required to produce a 55 N suspension force at least. As aforementioned in Table 1, the power of the designed motor is more than 1.5 kW and the rated speed is 15,000 r/min. Based on the design requirements, the optimization model can be presented as:

$$f(x_i)_{min} = \lambda_1\left(\alpha_1\frac{T_{out}}{T_{ave}} + \beta_1 T_{rip}\right) + \lambda_2\left(\alpha_2\frac{F_{min}}{F_{ave}} + \beta_2 F_{rip}\right) \tag{6}$$

$$\begin{aligned} &\min x_i \le x_i \le \max x_i,\ i = 1,2,3,.....n \\ &T_{(x_i)rip} = \frac{T_{(x_i)max} - T_{(x_i)min}}{T_{(x_i)ave}} \times 100\% \\ &F_{(x_i)rip} = \frac{F_{(x_i)max} - F_{(x_i)min}}{F_{(x_i)ave}} \times 100\% \end{aligned} \tag{7}$$

where T_{out} = 1 Nm, F_{min} = 55 N, x_i means the design variables, λ_1 and λ_2 are the weight coefficients of torque and suspension force, which satisfy the equation of $\lambda_1 + \lambda_2 = 1$, α_1 and β_1 are the weight coefficients of torque and torque ripple in the section of torque optimization, which satisfy the equation of $\alpha_1 + \beta_1 = 1$, α_2 and β_2 are the weight coefficients of suspension force and suspension force ripple in the section of suspension force optimization, which satisfy $\alpha_2 + \beta_2 = 1$. It is noted that, there are six weight coefficients of λ_1, λ_2, α_1, β_1, α_2 and β_2 in (6), and such weight coefficients usually represent the importance of optimization objectives. Generally, the choice of weight factors is always a key point in the process of multi-objective optimization [14,15]. However, there is not a single standard to determine the values of weight coefficients. In this paper, considering the same importance of the torque and suspension parts, the value of λ_1 and λ_2 are both selected to be 0.5. According to the design experience of conventional motors and the basic characteristics of bearingless motors, the weight factors of α_1, β_1, α_2 and β_2 are selected to be 0.4, 0.6, 0.4 and 0.6, respectively.

Figures 17–20 show the relationship between $f(x_i)_{min}$ and the optimization variables. So, as shown in Table 4, the rotor bar number is selected to be 34, the stator tooth shoe thickness is selected to be 0.35 mm, the stator pole arc coefficient is selected to be 0.95, R_a is designed to be 2 mm and L equals 6 mm in the proposed motor, respectively.

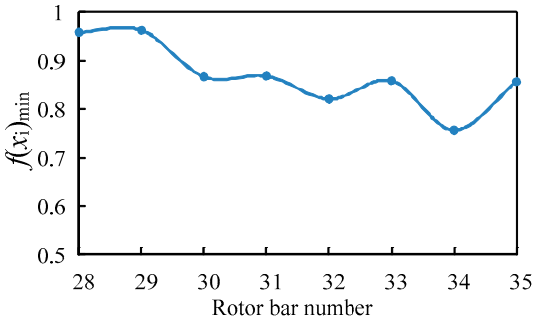

Figure 17. $f(x_i)_{min}$ versus rotor bar number.

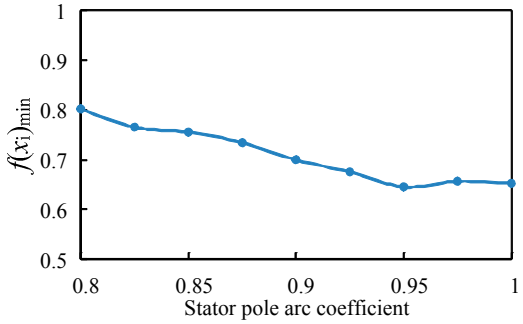

Figure 18. $f(x_i)_{min}$ versus stator pole arc coefficient.

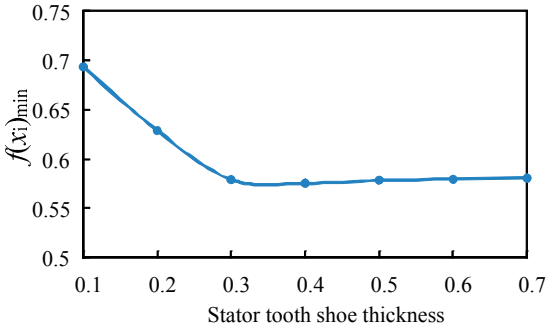

Figure 19. $f(x_i)_{min}$ versus stator tooth shoe thickness.

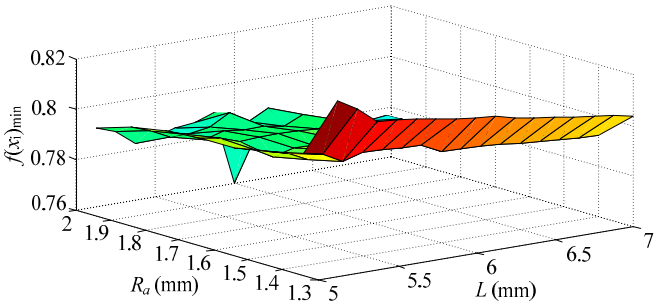

Figure 20. $f(x_i)_{min}$ versus bar dimensions.

Table 4. Initial values and optimal values.

Items	Initial Values	Optimal Values
Number of rotor bar	30	34
Stator pole arc coefficient, c	0.9	0.95
Stator tooth shoe thickness, t_s (mm)	0.4	0.35
Bar dimension, R_a (mm)	1.5	2
Bar dimension, L (mm)	5.5	6

4. Electromagnetic Performance Analysis

According to the aforementioned design procedure, the dimension parameters of the 3-phase BI motor with outer rotor can be obtained, and the corresponding key parameters are listed in Table 5. Then the electromagnetic performances of the designed motor can be calculated by using the FEA. In the FEA process, silicon steel M470-50A is adopted for the stator and rotor iron cores and the material of rotor bar is aluminum.

Table 5. Key parameters of proposed BI outer rotor motor.

Items	Values
TW pole-pair number, P_t	2
SW pole-pair number, P_s	1
Number of stator slot, Z	24
Number of rotor bar	34
Stator outer diameter, D_s (mm)	76
Stack length, la (mm)	70
Rotor outer diameter, D_r (mm)	114
Airgap, g_0 (mm)	0.3
Rated current of TW, i_s (A)	2.5
Rated current of SW, i_t (A)	2
Stator tooth shoe thickness, t_s (mm)	0.35
Stator pole arc coefficient, c	0.95
Bar dimension, R_a (mm)	2
Bar dimension, L (mm)	6

Figure 21 shows the suspension force and torque output waveforms when the rated currents are fed into the torque and SWs and the rotor is concentric with its stator. It can be seen that the average suspension force is 176 N and the suspension force ripple is 7.75%. In addition, the average torque is 1.1 Nm and torque ripple is 8.45%. Figure 22 shows the average suspension force variation waveforms with respect to the suspension current, when the torque current is equal to 2 A, 2.5 A and 3 A, respectively. It can be seen that the average suspension force is proportional to the suspension current, so it can be concluded that the suspension force can be controlled by adjusting the suspension current easily, which is consistent with (3). In addition, Figure 22 also describes the average torque variation waveforms with different currents of SW and TW. It shows that the torque increases along with torque current and suspension current, respectively, which is consistent with (4).

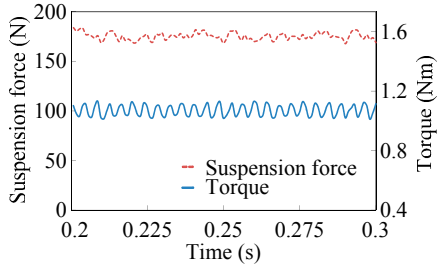

Figure 21. Waveforms of rated suspension force and torque.

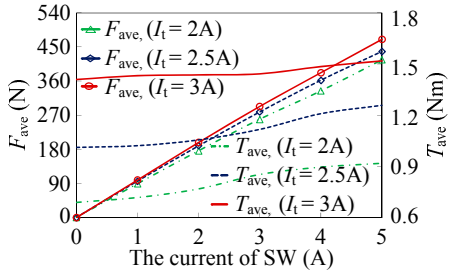

Figure 22. F_{ave} and T_{ave} versus suspension current and torque current.

Figure 23 shows the suspension force components of F_x and F_y when the rated currents are fed into the torque and SWs with different current phase θ, $\theta = \lambda - \mu$. It can be seen that the suspension force component of F_x is a cosine curve and the amplitude is 176 N. On the other hand, the suspension force component of F_y is a sine curve and the amplitude is also 176 N. So, F_x and F_y are basically

consistent with (2). When $\theta = 0°$, $F_x = 176$ N, and F_y is small enough to be ignored. Thus the resultant suspension force basically points to the positive direction of X-axis. So, it can be concluded that the angle between the resultant suspension force and X-axis is equal to $-\theta$, which is consistent with (2). Meanwhile, the relationship between F_x, F_y and the resultant suspension forces F_{ave} with θ can be represented as shown in Figure 24. It can be found that the direction of resultant suspension forces F_{ave} can be controlled by adjusting the current phase. In other words, by feeding currents with different phases into the SW and the TW, a suspension force in any direction can be obtained.

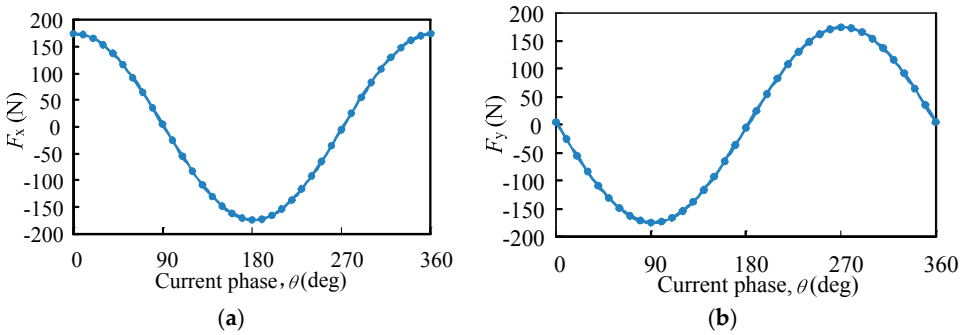

Figure 23. F_x and F_y versus current phase. (**a**) F_x versus current phase (**b**) F_y versus current phase.

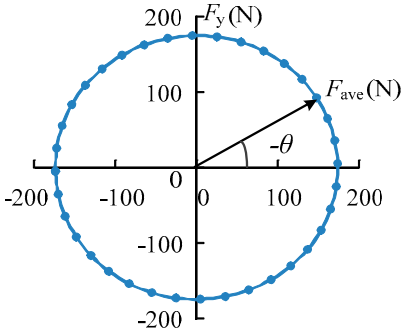

Figure 24. F_x, F_y and F_{ave} versus current phase.

In fact, the rotor will be decentered during motor operation. Therefore, when the rotor is radially decentered by external disturbances, the relationships between the radial suspension force, the torque and the eccentricity are investigated. Figure 25 shows the relationships between the torque and the rotor eccentricity in X- and Y-axis directions. It can be seen that when the rotor is shifted radially along the X-axis or Y-axis, the torque almost remains unchanged, namely the rotor eccentricity has little effect on the torque.

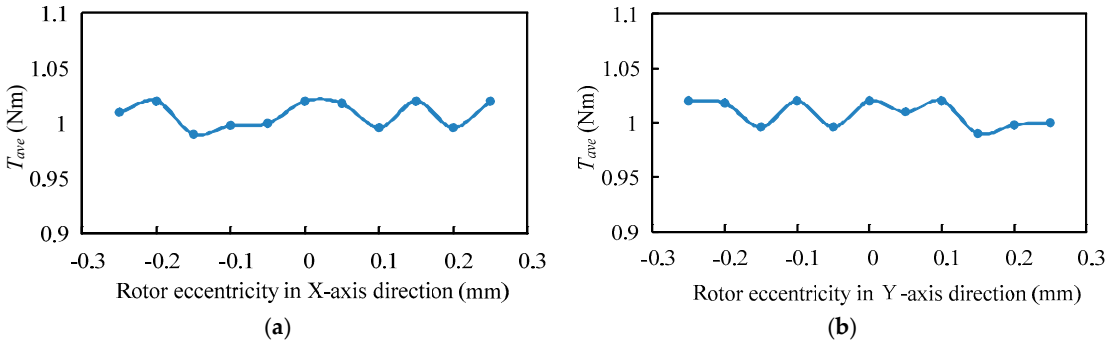

Figure 25. T_{ave} versus rotor eccentricity. (**a**) with eccentricity in X-axis direction; (**b**) with eccentricity in Y-axis direction.

Figure 26 shows the radial suspension force components and Figure 27 shows the resultant suspension force F_{ave} with different eccentricities in Y-axis direction. When the rated current is fed into both TW and SW with $\theta = 0°$ at rotor concentric position, the radial suspension force is $F_x = 176$ N and the resultant suspension force basically points to the positive direction of X-axis. However, a unilateral magnetic pull force will be produced in condition of rotor eccentricity [9]. As shown in Figure 26, when the rotor is shifted along the Y-axis, the radial suspension force in the Y-axis direction changes obviously because the motor airgap length in Y-axis is changed greatly. In addition, the amplitude of F_y is basically symmetrical with increasing rotor eccentricity y in different directions of Y-axis. The relationship between the radial suspension force F_y and the eccentric displacement y is close to linear. However, the amplitude of F_x changes in a very small range due the unchanged motor airgap length in X-axis direction. And the amplitude of F_x with the rotor eccentricity in Y-axis positive direction is slightly higher than that in the negative direction. So, the resultant suspension force F_{ave} is not symmetrical as shown in Figure 27.

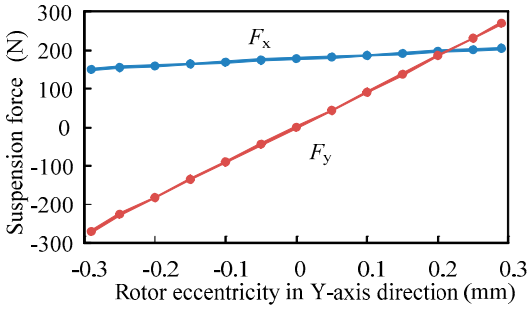

Figure 26. Suspension force versus rotor eccentricity in Y-axis direction.

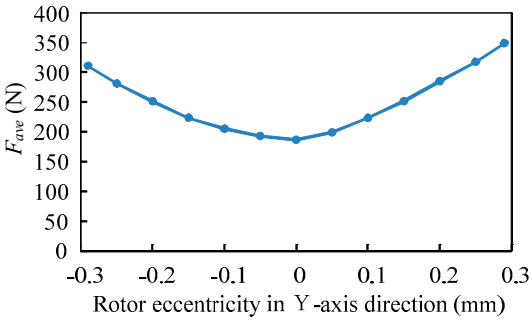

Figure 27. F_{ave} versus rotor eccentricity in Y-axis direction.

Figure 28 shows the radial suspension force components and Figure 29 shows the resultant suspension force F_{ave} with different eccentricities in X-axis direction. As can be seen from Figure 28, when the rotor is shifted along the X-axis, the radial suspension force in the X-axis direction is changed greatly. In addition, according to Equation (5), when the rotor is shifted towards the negative direction of X-axis, the radial force generated by the SW current is gradually offset by the unilateral magnetic pull force due to rotor eccentricity. So, with the increase of rotor eccentricity x in X-axis negative direction, the amplitude of F_x gradually decreases firstly, and then increases slowly in opposite direction due to the increasing unilateral magnetic pull force. When the rotor is shifted towards the positive direction of the X-axis, the radial force generated by the SW current is superimposed on the unilateral magnetic pull force caused by the rotor eccentricity. So the amplitude of F_x increases with increasing rotor eccentricity monotonously. As a result, the resultant suspension force F_{ave} gradually decreases firstly and then increases slowly, as shown in Figure 29.

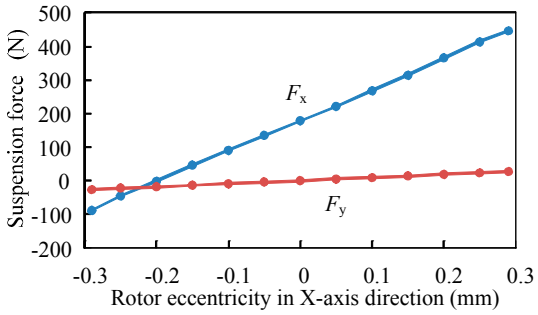

Figure 28. Suspension force versus rotor eccentricity in *X*-axis direction.

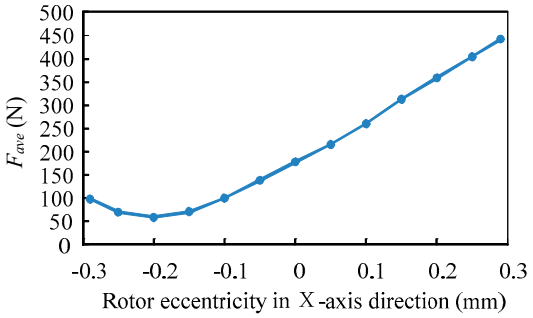

Figure 29. F_{ave} versus rotor eccentricity in *X*-axis direction.

In order to ensure a stable operation, the suspension force needs to be high enough to stably support the rotor. On other words, the radial force generated by the SW current can overcome rotor gravity and the unilateral magnetic pull force caused by the rotor eccentricity. In this paper, the motor rotor mass is 5.0 kg and the airgap between the rotating shaft and the auxiliary bearing is 0.12 mm. So, the eccentricity of rotor is limited within 0.12 mm. As can be seen from Figure 28, when the rated currents are fed into both TW and SW with $\theta = 0°$ and the rotor shifts -0.12 mm in *X*-axis direction, F_x reaches 91.6 N in the positive direction of the *X*-axis. In other words, the suspension force produced by suspension current can overcome the unilateral magnetic pull force caused by rotor eccentricity, and there is still a radial force of 91.6 N that can be used to achieve the rotor suspension. Similarly, combining with Figures 23, 24 and 28 and the symmetry of motor structure, it can be found that when the rated current is fed into both TW and SW with $\theta = -90°$, and the rotor reaches -0.12 mm in *Y*-axis direction, F_{Y} is 91.6 N. Considering the rotor weight of 5.0 kg, there is a radial force of 41.6 N that can be used to pull the rotor back to the balance position. Therefore, the motor designed in this paper can be suspended in the case of rotor eccentricity.

5. Conclusions

In this paper, a BI motor with outer rotor has been designed and analyzed. Firstly, the configuration of the BI motor is presented and its torque and suspension force production mechanisms are discussed. In order to obtain the maximum torque and suspension force and the minimum torque ripple and suspension force ripple, several key parameters are optimally designed by using the FEA. The results of FEA show that the suspension force depends strongly on the airgap. The stator pole arc coefficient and the stator pole shoe thickness have little influence on the suspension force, and have an important influence on the torque and torque ripple. In addition, it can be used to optimize the suspension force and torque ripple effectively by selecting the appropriate rotor bar number. Based on the FEA, the electromagnetic performances of the proposed motor with optimal dimensions are calculated and analyzed. When the rated currents are fed into both TW and SW, the suspension force is 176 N and the suspension force ripple is 7.75%. The suspension force is able to overcome the gravity of rotor and

the unilateral magnetic pull force caused by rotor eccentricity. At the same time, the average torque is 1.1 Nm and the torque ripple is 8.45%, which can meet the motor design requirements. Finally, the effect of rotor eccentricity on the torque and suspension force are investigated. As shown in the simulation results, the torque output is basically unchanged in the case of rotor eccentricity. The rotor radial displacements along the X-axis and Y-axis mainly affect the radial forces in X-axis and Y-axis directions, respectively. Moreover, in the case of rotor eccentricity, the motor can be suspended stably.

Acknowledgments: This work was sponsored by National Natural Science Foundation of China (51675244), Key Research and Development Project of Jiangsu Province (BE2016150) and the grant from the Priority Academic Program Development of Jiangsu Higher Education Institution.

Author Contributions: All authors contributed to this work by collaboration. Yuxin Sun, Jingwei Tang and Kai Shi are the main authors of this manuscript.

Conflicts of Interest: The authors declare no conflict of interest.

References

1. Gerada, D.; Mebarki, A.; Brown, N.L.; Gerada, C. High-speed electrical machines: Technologies, trends, and developments. *IEEE Trans. Ind. Electron.* **2014**, *61*, 2946–2959. [CrossRef]
2. He, Y.; Nian, H. Analytical model and feedback control of the suspension force for an induction type bearingless motor. *IEEE Proc. PEDS* **2003**, *1*, 242–246. [CrossRef]
3. Bu, W.; Huang, S.; Wan, S.; Liu, W. General analytical models of inductance matrices of four-pole bearingless motors with two-pole controlling windings. *IEEE Trans. Magn.* **2009**, *45*, 3316–3321. [CrossRef]
4. Reichert, T.; Nussbaumer, T.; Gruber, W.; Kolar, J.W. Bearingless permanent-magnet motor with 4/12 slot-pole ratio for bioreactor stirring applications. *IEEE/ASME Trans. Mechatron.* **2011**, *16*, 431–439. [CrossRef]
5. Li, W.; Chau, K.T.; Ching, T.W.; Wang, Y.; Chen, M. Design of a high-speed superconducting bearingless machine for flywheel energy storage systems. *IEEE Trans. Appl. Supercond.* **2015**, *25*, 5700204. [CrossRef]
6. Cao, X.; Deng, Z. A full-period generating mode for bearingless switched reluctance generators. *IEEE Trans. Appl. Supercond.* **2010**, *20*, 1072–1076. [CrossRef]
7. Chiba, A.; Asama, J. Influence of rotor skew in induction type bearingless motor. *IEEE Trans. Magn.* **2012**, *48*, 4646–4649. [CrossRef]
8. Ferreira, J.M.S.; Zucca, M.; Salazar, A.O.; Donadio, L. Analysis of a bearingless machine with divided windings. *IEEE Trans. Magn.* **2005**, *41*, 3931–3933. [CrossRef]
9. Schoeb, R.; Bichsel, J. Vector control of the bearingless motor. In Proceedings of the International Symposium on Magnetic Bearings (ISMB), ETH Zurich, Zürich, Switzerland, 23–26 August 1994.
10. Pyrhoenen, J.; Jokinen, T.; Hrabovcova, V. *Design of Rotating Electrical Machines*; John Wiley & Sons: New Dehli, India, 2013; ISBN: 9780470695166.
11. Zheng, P.; Liu, R.; Thelin, P.; Nordlund, E. Research on the cooling system of a 4QT prototype machine used for HEV. *IEEE Trans. Energy Convers.* **2008**, *50*, 61–67. [CrossRef]
12. Lei, G.; Wang, T.; Guo, Y.; Zhu, J. System-level design optimization methods for electrical drive systems: Deterministic approach. *IEEE Trans. Ind. Electron.* **2014**, *61*, 6591–6602. [CrossRef]
13. Zhu, X.; Shu, Z.; Quan, L.; Xiang, Z. Multi-objective optimization of an outer-rotor V-shaped permanent magnet flux switching motor based on multi-level design method. *IEEE Trans. Magn.* **2016**, *52*, 8205508. [CrossRef]
14. Lei, G.; Liu, C.; Zhu, J.; Guo, Y. Techniques for multilevel design optimization of permanent magnet motors. *IEEE Trans. Energy Convers.* **2015**, *30*, 1574–1584. [CrossRef]
15. Lei, G.; Xu, W.; Hu, J.; Zhu, J. Multilevel design optimization of a FSPMM drive system by using sequential subspace optimization method. *IEEE Trans. Magn.* **2014**, *50*, 685–688. [CrossRef]